Title

A model for describing phase-converted image intensity noise in digital fringe projection techniques

Authors

O'Dowd, Niall M
Wachtor, Adam J
Todd, Michael D

Publication Date

2020-11-01

DOI

10.1016/j.optlaseng.2020.106293

Peer reviewed

A MODEL FOR DESCRIBING PHASE-CONVERTED IMAGE INTENSITY NOISE IN DIGITAL FRINGE PROJECTION TECHNIQUES

Niall M. O'Dowd[1], Adam J. Wachtor[2], and Michael D. Todd[3]

[1,3]Department of Structural Engineering, University of California San Diego
[2]Engineering Institute, Los Alamos National Laboratory
[1]nmodowd@eng.ucsd.edu, [2]ajw@lanl.gov, [3]mdtodd@eng.ucsd.edu (corresponding author)

Key words: Digital Fringe Projection; Phase Estimation; Noise Transfer Model

Abstract. Digital fringe projection is a surface-profiling technique that is gaining popularity due to the increasing availability and quality of low-cost projection equipment and digital cameras. Noise in the pixel field of imaged targets induces error in the reconstructed phase and ultimately the surface profile measurement. In this paper, we present an approximate analytical probability density function for the estimated phase given an arbitrarily-correlated Gaussian pixel noise structure. This probability density function can be used to estimate the single point phase measurement uncertainty from easily obtainable pixel intensity noise statistics. We confirm the accuracy of the new model by comparing it to a Monte-Carlo simulation of the phase distribution. A complimentary graphics model is proposed which simulates the physical process of full-field phase measurement using a pin-hole camera model and three-dimensional point clouds of the measurement surface, allowing for another level of model verification.

1 Introduction

Digital fringe projection (DFP) is a technique which is widely used to perform certain measurements, including shape sensing and texture assessment [1]. It is comprised of a structured light system with (at minimum) three components: a camera, a projector, and a computer. DFP's early predecessor, pattern interference analysis, began with investigation of Moiré patterns such as in [2–6]. Electronic speckle pattern interferometry was developed shortly thereafter, as in [7, 8], to produce controlled and dynamic interference patterns for measuring strain deflections and other small scale displacements. DFP was born from the concepts of these optical interference techniques and the advancement of the portable projector, where the interference patterns can simply be projected with white, non-collimated, non-polarized light. Applications for DFP are widely varying, and can be found in fields such as biomedical [9–11], material science [12–14], and electronics inspection [15, 16].

Several sources of error effect the accuracy of DFP measurement, including nonlinear projector gamma [17–19], phase-to-height calibration error [20, 21], and pixel intensity noise caused by fluctuation in environmental lighting during DFP measurement and electronic noise within the camera and projector [22–25]. The current work is focused on quantifying phase error converted from pixel intensity noise, a source of error affecting a wide range of profiling techniques [23]. Unlike other sources of error, pixel noise error contributions are unavoidable despite the optimization of DFP system setup [22]. A study by G. Notni et al. has reported that pixel noise error is large enough to dwarf the error contribution from spatial and intensity quantification [26], and techniques which aim to reduce the contribution of pixel intensity noise have been explored in [24, 25] where new phase shifting algorithms

were proposed to mitigate pixel error. However, none of these works undertook a rigorous measurement model of the measurement process in which pixel intensity gets phase converted (and thus, ultimately, leads to height measurement error). There has been substantial work done on analyzing the inherent error caused by nonlinear projector gamma [17–19] and the effect of linearizing the phase-to-height transformation [20, 21]. However, to the authors' knowledge and assessment of the open literature, there are no studies that provide single-point phase measurement uncertainty analysis from pixel intensity noise in the DFP application space. The work of G. Notni et al. [26] summarized a variety of quantization errors due to the nature of the digital camera and projector in DFP phase measurement, but it did not include phase-converted pixel intensity noise analysis nor an analytically derived model for the phase measurement dispersion caused by the quantization errors.

Though previous work generating a three-dimensional (3D) graphics model to mimic the experimental process of DFP has been published, these authors have not used their models to analyze phase measurement error using Monte-Carlo simulations to generate model inputs for pixel noise. A study done by J. Molimard et. al, used a Monte-Carlo framework in attempt to quantify the phase measurement error caused by phase-to-height calibration [27], but not the phase distribution error based on input pixel noise. Thus, the work presented in this study advances the DFP measurement field by deriving the statistical uncertainty model for single-point phase measurement from pixel intensity noise. This model is verified against a Monte-Carlo perturbation simulation with varying degrees of cross-pixel noise correlation, and a 3D graphics model for ensuring that assumptions made regarding the carrier phase are valid. The purpose of developing these models is to create a method to estimate the point-wise phase measurement uncertainty by using quantifiable and easy-to-measure pixel noise statistics.

In the DFP measurement process, these phase measurements are made by projecting a series of patterns onto a scene and recording the resulting deformation of the patterns caused by the measured object. A schematic of the fringe deformation process in shown in Figure 1, where the phase (related to height) of point Q is to be measured. A common implementation of DFP is, essentially, a differential phase measurement; a series of fringe images are first projected onto a flat reference plane (mathematical or physical, denoted by the subscript r in Figure 1), and then placing the measurement object (denoted by the subscript o in Figure 1) into the scene, which deforms the incident projected fringe pattern. The camera records images of the incident fringes on both surfaces, where the intensity $I_{(r,o)}$ of any fringe incident on the measurement surface (either r or o) at any given location $x_{r,o}$ is given by [28]

$$I_{(r,o)} = A_{(r,o)} + B_{(r,o)} \cos\left(2\pi x_{(r,o)}/P\right), \tag{1}$$

where $\phi_{(r,o)} = 2\pi x_{(r,o)}/P$ is the fringe phase, P is the fringe pitch, and $A_{(r,o)}$ and $B_{(r,o)}$ are the ambient light intensity and the projected fringe contrast, respectively, at the arbitrary point $x_{(r,o)}$. In order to recover differential information between object and reference phases, which is functionally related to the object height [29], N phase-shifted images are generated and projected onto both reference and object with (equipartitioned) spatial shifts $\delta_k = 2\pi k/N$, $k = 1...N$ (often called "bins"), such that the intensities in Equation 1 may be each written as

$$I_{(r,o),k} = A_{(r,o),k} + B_{(r,o),k} \cos\left(\phi_{(r,o)} + \delta_k\right), \tag{2}$$

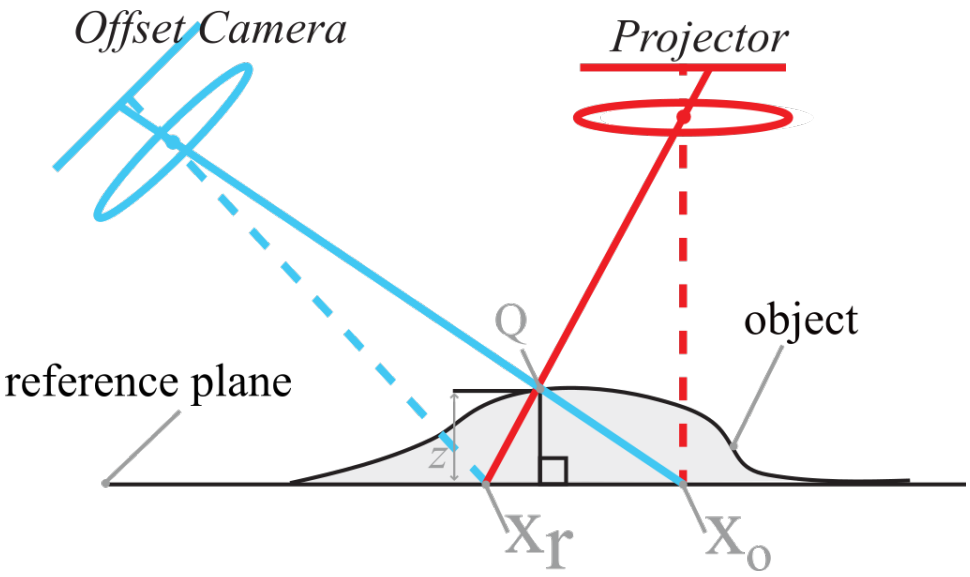

Figure 1: A general schematic of reference based fringe projection.

and it may be readily shown that the individual phases at the point of interest are recovered by

$$\phi_{(r,o)} = \arctan\left(\frac{-\sum_{k=1}^{N} I_{(r,o),k}\sin\delta_k}{\sum_{k=1}^{N} I_{(r,o),k}\cos\delta_k}\right), \tag{3}$$

if the projected fringe intensities are evenly spaced without nonlinear projector gamma issues. The final required differential phase measurement (referred onward as true phase) ϕ between object and reference is given by

$$\begin{aligned}\phi &= \phi_o - \phi_r \\ &= \arctan\left(\frac{-\sum_{k=1}^{N} I_{o,k}\sin\delta_k}{\sum_{k=1}^{N} I_{o,k}\cos\delta_k}\right) - \arctan\left(\frac{-\sum_{k=1}^{N} I_{r,k}\sin\delta_k}{\sum_{k=1}^{N} I_{r,k}\cos\delta_k}\right) \qquad (4)\\ &= \frac{2\pi\left(x_o - x_r\right)}{P}. \qquad (5)\end{aligned}$$

Equation 5 represents the exact phase that is related (proportionally, under some projection assumptions) to the height of the object. In this article, we will not be exploring the subsequent relationship between phase and object height, which is discussed thoroughly in [29]. The fundamental objective of this work going forward is to develop a model that statistically characterizes the true phase ϕ estimated by the process in Equations 2-5 when the images from Equation 2 have arbitrarily-correlated Gaussian noise.

2 Single Point DFP Phase Noise Model

2.1 Output Phase Noise Formulation

The idealized intensity formulation presented in Equation 2 may be modified in both reference and object images to account for pixel noise. Assuming the noise may be modeled additively to the idealized intensities, the i-th and j-th image intensities of the reference and object images, respectively,

taken from the reference and object location $x_{r,o}$, are given by

$$\begin{aligned} I_{r,i} &= A_r + B_r \cos\left(2\pi x_r/P + 2\pi i/N + \phi_c\right) + \epsilon_{r,i}, i = 1...N \quad (6) \\ I_{o,j} &= A_o + B_o \cos\left(2\pi x_o/P + 2\pi j/N + \phi_c\right) + \epsilon_{o,j} \\ &= A_o + B_o \cos\left(2\pi x_r/P + \phi + 2\pi j/N + \phi_c\right) + \epsilon_{o,j}, j = 1...N, \quad (7) \end{aligned}$$

where we have used the definition of ϕ from Equation 5. We added the term ϕ_c to account for the spatial phase offset of the measurement point in relation to the projected fringe pattern. The current work focuses on deriving the single-point phase measurement distribution, and since x_r is completely arbitrary, we may choose $x_r = 0$ without loss of generality in subsequent analysis. Inserting Equations 6 and 7 into Equation 4, we obtain the measured/estimated differential phase ϕ_m, after employing the difference-of-arctangents trigonometric formula:

$$\begin{aligned} \phi_m &= -\arctan\left(\frac{\sum_{i,j=1}^{N}\sin\left(\frac{2\pi(i-j)}{N}\right)\left(A_o + B_o\cos\left(\frac{2\pi i}{N}+\phi+\phi_c\right)+\epsilon_{o,i}\right)\left(A_r + B_r\cos\left(\frac{2\pi j}{N}+\phi_c\right)+\epsilon_{r,j}\right)}{\sum_{i,j=1}^{N}\cos\left(\frac{2\pi(i-j)}{N}\right)\left(A_o + B_o\cos\left(\frac{2\pi i}{N}+\phi+\phi_c\right)+\epsilon_{o,i}\right)\left(A_r + B_r\cos\left(\frac{2\pi j}{N}+\phi_c\right)+\epsilon_{r,j}\right)}\right) \\ &= \arctan\left(\frac{\sin\phi + \frac{2}{N}\sum_{i=1}^{N}\sin\left(\frac{2\pi i}{N}+\phi+\phi_c\right)\frac{\epsilon_{r,i}}{B_r} - \sin\left(\frac{2\pi i}{N}+\phi_c\right)\frac{\epsilon_{o,i}}{B_o} - \frac{4}{N^2}\sum_{i,j=1}^{N}\sin\left(\frac{2\pi(i-j)}{N}\right)\frac{\epsilon_{o,i}}{B_o}\frac{\epsilon_{r,j}}{B_r}}{\cos\phi + \frac{2}{N}\sum_{i=1}^{N}\cos\left(\frac{2\pi i}{N}+\phi+\phi_c\right)\frac{\epsilon_{r,i}}{B_r} + \cos\left(\frac{2\pi i}{N}+\phi_c\right)\frac{\epsilon_{o,i}}{B_o} + \frac{4}{N^2}\sum_{i,j=1}^{N}\cos\left(\frac{2\pi(i-j)}{N}\right)\frac{\epsilon_{o,i}}{B_o}\frac{\epsilon_{r,j}}{B_r}}\right). \end{aligned} \quad (8)$$

We see that each intensity noise term scales by its respective fringe contrast so that we may redefine a scaled noise as $\overline{\epsilon}_{o,i} = \epsilon_{o,i}/B_o$, $\overline{\epsilon}_{r,i} = \epsilon_{r,i}/B_r$, and $\overline{\epsilon}_{r,j} = \epsilon_{r,j}/B_r$. It is clear that if all input noise is zero, i.e., $\epsilon_{r,i} = \epsilon_{r,j} = \epsilon_{o,i} = 0$, then $\phi_m = \arctan\left(\sin\phi/\cos\phi\right) = \phi$, as would be expected.

Finally, we define the residual phase measurement noise as $\kappa = \phi_m - \phi$, which may be written, after again using the difference-in-arctangents formula and performing some mathematical manipulations,

$$\kappa = \arctan\left(\frac{\frac{2}{N}\sum_{i=1}^{N}\sin\left(\frac{2\pi i}{N}+\phi_c\right)\overline{\epsilon}_{r,i} - \sin\left(\frac{2\pi i}{N}+\phi+\phi_c\right)\overline{\epsilon}_{o,i} - \frac{4}{N^2}\sum_{i,j=1}^{N}\sin\left(\frac{2\pi(i-j)}{N}+\phi\right)\overline{\epsilon}_{o,i}\overline{\epsilon}_{r,j}}{1 + \frac{2}{N}\sum_{i=1}^{N}\cos\left(\frac{2\pi i}{N}+\phi_c\right)\overline{\epsilon}_{r,i} + \cos\left(\frac{2\pi i}{N}+\phi+\phi_c\right)\overline{\epsilon}_{o,i} + \frac{4}{N^2}\sum_{i,j=1}^{N}\cos\left(\frac{2\pi(i-j)}{N}+\phi\right)\overline{\epsilon}_{o,i}\overline{\epsilon}_{r,j}}\right). \quad (9)$$

Equation 9 is an exact noise transfer function, converting reference and object image intensity noise to output phase noise. As above, we observe that if all of the $\overline{\epsilon}$ terms are zero, then $\kappa = 0$, as expected. We note that the last term in both numerator and denominator are of order $\overline{\epsilon}^2$; for all practical scaled noise values, these terms are negligible compared to the other terms, so we may express an approximate noise transfer function as

$$\kappa \approx \arctan\left(\frac{\frac{2}{N}\sum_{i=1}^{N}\sin\left(\frac{2\pi i}{N}+\phi_c\right)\overline{\epsilon}_{r,i} - \sin\left(\frac{2\pi i}{N}+\phi+\phi_c\right)\overline{\epsilon}_{o,i}}{1 + \frac{2}{N}\sum_{i=1}^{N}\cos\left(\frac{2\pi i}{N}+\phi_c\right)\overline{\epsilon}_{r,i} + \cos\left(\frac{2\pi i}{N}+\phi+\phi_c\right)\overline{\epsilon}_{o,i}}\right). \quad (10)$$

Our subsequent goal is to find a probability density function (PDF) $p(\kappa)$, based on the approximate (but still retaining fundamental nonlinearity) transfer function given in Equation 10, given arbitrarily-correlated Gaussian intensity noise structure among and between the $\overline{\epsilon}_{o,i}$ and $\overline{\epsilon}_{r,i}$.

2.2 Probability Density Function Model

We begin our model derivation by first assuming formally that the pixel intensity noise for the reference and the object images are each jointly normally distributed [30–32], allowing arbitrary image-to-image correlation, i.e., $\overline{\epsilon}_{r,i} \sim N\left(\mu_{r,i}, \sigma_{r,i}, \Sigma_{r,ij}\right)$ and $\overline{\epsilon}_{o,i} \sim N\left(\mu_{o,i}, \sigma_{o,i}, \Sigma_{o,ij}\right)$, $i = 1...N$, where μ is the pixel intensity noise mean, σ is the pixel intensity noise standard deviation, and Σ is the image-to-image pixel intensity noise correlation. We also generally assume that the reference and object images could also be correlated with correlation matrix $\Sigma_{or,ij}$; in other words, this allows for the (general) possibility that the i-th object image noise could be correlated with the j-th reference image noise (in addition to the initial assumption that individual reference and object images may be intra-correlated). Thus, a global correlation matrix Σ_{ij} could be constructed as

$$\Sigma_{ij} = \begin{bmatrix} \Sigma_{o,ij} & \Sigma_{or,ij} \\ \Sigma_{ro,ij} & \Sigma_{r,ij} \end{bmatrix}. \tag{11}$$

The upper left and lower right square sub-matrices describe the intra-image correlation structure in the object and reference images, respectively, while the upper right and lower left sub-matrices describe any correlation structure between object and reference images. The following expectation operations, where $E\left[*\right]$ is the expectation operator, are defined as

$$\begin{aligned} E\left[\overline{\epsilon}_{r,i}\right] &= \mu_{r,i} \\ E\left[\overline{\epsilon}_{o,i}\right] &= \mu_{o,i} \\ E\left[\overline{\epsilon}_{o,i}\overline{\epsilon}_{o,j}\right] &= \mu_{o,i}\mu_{o,j} + \rho_{o,ij}\sigma_{o,i}\sigma_{o,j} \\ E\left[\overline{\epsilon}_{r,i}\overline{\epsilon}_{r,j}\right] &= \mu_{r,i}\mu_{r,j} + \rho_{r,ij}\sigma_{r,i}\sigma_{r,j} \\ E\left[\overline{\epsilon}_{o,i}\overline{\epsilon}_{r,j}\right] &= \mu_{o,i}\mu_{r,j} + \rho_{or,ij}\sigma_{o,i}\sigma_{r,j}, \end{aligned} \tag{12}$$

where $\Sigma_{r,ij} = \rho_{r,ij}\sigma_{r,i}\sigma_{r,j}$, $\Sigma_{o,ij} = \rho_{o,ij}\sigma_{o,i}\sigma_{o,j}$, $\Sigma_{or,ij} = \rho_{or,ij}\sigma_{o,i}\sigma_{r,j}$, while ρ_* is a correlation coefficient and σ_* is a standard deviation.

We note that the form of Equation 10 could be written as $\kappa = \arctan\left(Y/X\right)$, where the numerator Y and denominator X are given by

$$\begin{aligned} Y &= \frac{2}{N}\sum_{i=1}^{N} \sin\left(\frac{2\pi i}{N} + \phi_c\right)\overline{\epsilon}_{r,i} - \sin\left(\frac{2\pi i}{N} + \phi + \phi_c\right)\overline{\epsilon}_{o,i} \\ X &= 1 + \frac{2}{N}\sum_{i=1}^{N} \cos\left(\frac{2\pi i}{N} + \phi_c\right)\overline{\epsilon}_{r,i} + \cos\left(\frac{2\pi i}{N} + \phi + \phi_c\right)\overline{\epsilon}_{o,i}. \end{aligned} \tag{13}$$

Both Y and X are just weighted sums of Gaussian variables, so the probability density functions of Y and X will remain Gaussian; we take expectations of Y and X in order to calculate the mean values associated with their Gaussian densities, μ_Y and μ_X:

$$\begin{aligned} \mu_Y &= E\left[Y\right] \\ &= \frac{2}{N}\sum_{i=1}^{N} \sin\left(\frac{2\pi i}{N} + \phi_c\right)E\left[\overline{\epsilon}_{r,i}\right] - \sin\left(\frac{2\pi i}{N} + \phi + \phi_c\right)E\left[\overline{\epsilon}_{o,i}\right] \end{aligned}$$

$$= \frac{2}{N}\sum_{i=1}^{N}\sin\left(\frac{2\pi i}{N}+\phi_c\right)\mu_{r,i} - \sin\left(\frac{2\pi i}{N}+\phi+\phi_c\right)\mu_{o,i} \quad (14)$$

$$\begin{aligned}\mu_X &= E[X] \\ &= 1+\frac{2}{N}\sum_{i=1}^{N}\cos\left(\frac{2\pi i}{N}+\phi_c\right)E[\bar{\epsilon}_{r,i}] + \cos\left(\frac{2\pi i}{N}+\phi+\phi_c\right)E[\bar{\epsilon}_{o,i}] \\ &= 1+\frac{2}{N}\sum_{i=1}^{N}\cos\left(\frac{2\pi i}{N}+\phi_c\right)\mu_{r,i} + \cos\left(\frac{2\pi i}{N}+\phi+\phi_c\right)\mu_{o,i}. \end{aligned} \quad (15)$$

Similarly, we compute the variances of Y and X, $\sigma_Y^2 = E[Y^2] - E^2[Y]$ and $\sigma_X^2 = E[X^2] - E^2[X]$, by taking appropriate expectations:

$$\begin{aligned}\sigma_Y^2 &= \frac{4}{N^2}\sum_{i,j=1}^{N}\sin\left(\frac{2\pi i}{N}+\phi+\phi_c\right)\sin\left(\frac{2\pi j}{N}+\phi+\phi_c\right)E[\bar{\epsilon}_{o,i}\bar{\epsilon}_{o,j}] \\ &-2\sin\left(\frac{2\pi i}{N}+\phi+\phi_c\right)\sin\left(\frac{2\pi j}{N}+\phi_c\right)E[\bar{\epsilon}_{o,i}\bar{\epsilon}_{r,j}] + \sin\left(\frac{2\pi i}{N}+\phi_c\right)\sin\left(\frac{2\pi j}{N}+\phi_c\right)E[\bar{\epsilon}_{r,i}\bar{\epsilon}_{r,j}] - \mu_Y^2 \\ &= \frac{4}{N^2}\sum_{i,j=1}^{N}\sin\left(\frac{2\pi i}{N}+\phi+\phi_c\right)\sin\left(\frac{2\pi j}{N}+\phi+\phi_c\right)\rho_{o,ij}\sigma_{o,i}\sigma_{o,j} \\ &-2\sin\left(\frac{2\pi i}{N}+\phi+\phi_c\right)\sin\left(\frac{2\pi j}{N}+\phi_c\right)\rho_{or,ij}\sigma_{o,i}\sigma_{r,j} + \sin\left(\frac{2\pi i}{N}+\phi_c\right)\sin\left(\frac{2\pi j}{N}+\phi_c\right)\rho_{r,ij}\sigma_{r,i}\sigma_{r,j}. \end{aligned} \quad (16)$$

The derivation of the terms $E[Y^2]$ and $E^2[Y]$ employed usage of a double sum across indices i, j in $\sum_{i,j=1}^{N}$ to indicate the product of two series. Similarly,

$$\begin{aligned}\sigma_X^2 &= \frac{4}{N^2}\sum_{i,j=1}^{N}\cos\left(\frac{2\pi i}{N}+\phi+\phi_c\right)\cos\left(\frac{2\pi j}{N}+\phi+\phi_c\right)\rho_{o,ij}\sigma_{o,i}\sigma_{o,j} \\ &+2\cos\left(\frac{2\pi i}{N}+\phi+\phi_c\right)\cos\left(\frac{2\pi j}{N}+\phi_c\right)\rho_{or,ij}\sigma_{o,i}\sigma_{r,j} + \cos\left(\frac{2\pi i}{N}+\phi_c\right)\cos\left(\frac{2\pi j}{N}+\phi_c\right)\rho_{r,ij}\sigma_{r,i}\sigma_{r,j}. \end{aligned} \quad (17)$$

Finally, since X and Y are in general correlated, we compute their covariance $\mathrm{cov}[X,Y] = E[XY] - E[X]E[Y]$ as

$$\begin{aligned}\mathrm{cov}(X,Y) &= -\frac{4}{N^2}\sum_{i,j=1}^{N}\sin\left(\frac{2\pi i}{N}+\phi+\phi_c\right)\cos\left(\frac{2\pi j}{N}+\phi+\phi_c\right)\rho_{o,ij}\sigma_{o,i}\sigma_{o,j} \\ &+\sin\left(\frac{2\pi(i-j)}{N}+\phi\right)\rho_{or,ij}\sigma_{o,i}\sigma_{r,j} - \sin\left(\frac{2\pi i}{N}+\phi_c\right)\cos\left(\frac{2\pi j}{N}+\phi_c\right)\rho_{r,ij}\sigma_{r,i}\sigma_{r,j}. \end{aligned} \quad (18)$$

The covariance between X and Y is composed of contributions from possible intra-image correlation within the reference and object images ($\rho_{o,ij}$ and $\rho_{r,ij}$), as well as reference-to-object image correlation ($\rho_{or,ij}$). In general, all the order statistics of X and Y depend on input noise statistical parameters as well as the true phase ϕ.

Thus, we may conclude that X and Y are jointly normally distributed, with individual means μ_X and μ_Y, variances σ_X^2 and σ_Y^2, and correlation coefficient $\rho_{XY} = \mathrm{cov}(X,Y)/\sqrt{\sigma_X\sigma_Y}$, all given by

Equations 14-18, such that their joint probability density function may be given by

$$p\left(X,Y\right)=\frac{1}{2\pi\sigma_X\sigma_Y\sqrt{1-\rho_{XY}^2}}e^{\frac{-1}{2\left(1-\rho_{XY}^2\right)}\left(\frac{(X-\mu_X)^2}{\sigma_X^2}+\frac{(Y-\mu_Y)^2}{\sigma_Y^2}-\frac{2\rho_{XY}(X-\mu_X)(Y-\mu_Y)}{\sigma_X\sigma_Y}\right)}. \tag{19}$$

Now that we have the joint density for X and Y, we can use the change-of-variables technique by making a coordinate transformation $X=X$ and $\kappa=\arctan\left(Y/X\right)$ so that we obtain the probability density function of κ explicitly as

$$\begin{aligned} p(\kappa) &= \int_{-\infty}^{\infty}\frac{p(X,Y)}{|\partial\kappa/\partial Y|}dX \\ &= \int_{-\infty}^{\infty}\frac{p(X,Y)}{|X/\left(X^2+Y^2\right)|}dX \\ &= \int_{-\infty}^{\infty}p(X,X\tan\kappa)|X|\sec^2\kappa dX, \end{aligned} \tag{20}$$

since $Y=X\tan\kappa$.

The integrand and integration range in Equation 20 require separation into two regions, one for the case $X>0$ ($|\kappa|<\pi/2$) and for the case $X<0$ ($\pi>|\kappa|>\pi/2$). Both integrations admit closed-form solutions, given by

$$p\left(\kappa\right)=\frac{e^{-z_3}\sec^2\kappa\left(1+\sqrt{\pi}z_2e^{z_2^2}\left(\mathrm{erf}\left(z_2\right)\pm1\right)\right)}{2\pi z_1\sqrt{1-\rho_{XY}^2}}, \tag{21}$$

where

$$\begin{aligned} z_1 &= \frac{\sigma_Y^2-2\rho_{XY}\sigma_X\sigma_Y\tan\kappa+\sigma_X^2\tan^2\kappa}{\sigma_X\sigma_Y\left(1-\rho_{XY}^2\right)}, \\ z_2 &= \frac{\mu_Y\sigma_X\left(\rho_{XY}\sigma_Y-\sigma_X\tan\kappa\right)+\mu_X\sigma_Y\left(\sigma_X\rho_{XY}\tan\kappa-\sigma_Y\right)}{\sqrt{2}\sigma_X\sigma_Y\sqrt{1-\rho_{XY}^2}\sqrt{\sigma_Y^2-2\rho_{XY}\sigma_X\sigma_Y\tan\kappa+\sigma_X^2\tan^2\kappa}}, \\ z_3 &= \frac{\mu_Y^2\sigma_X^2+\mu_X^2\sigma_Y^2-2\mu_X\mu_Y\sigma_X\sigma_Y\rho_{XY}}{2\sigma_X^2\sigma_Y^2\left(1-\rho_{XY}^2\right)}, \end{aligned} \tag{22}$$

and $\mathrm{erf}(*)$ is the standard error function. The minus $(-)$ sign is taken in Equation 21 when $|\kappa|<\pi/2$ (when $X>0$), while the plus $(+)$ sign is taken when $\pi>|\kappa|>\pi/2$ (when $X<0$).

2.3 Special Case

While Equation 21 together with the definitions in Equation 22 completely determine the probability density function of κ for any arbitrarily-correlated pixel intensity noise, one special case should be mentioned. If no correlation exists between the pixel intensity noise of phase shifted images within either the object or the reference images, i.e., $\rho_{o,ij}=\rho_{r,ij}=\delta_{ij}$ (the identity matrix, where $\delta_{ij}=0$ for $i\neq j$ and $\delta_{ij}=1$ for $i=j$), no correlation exists between the images of the reference and object, i.e. $\rho_{or,ij}=0$ for all i and j, the intensity noise is unbiased, i.e., $\mu_{o,i}=\mu_{r,i}=0$, and the noise standard deviations in each object and each reference image are the same for all images, i.e., $\sigma_{o,i}=\sigma_o$

and $\sigma_{r,i} = \sigma_r$, then the order statistics for X and Y reduce to

$$\begin{aligned} \mu_Y &= 0 \\ \mu_X &= 1 \\ \sigma_Y^2 &= \frac{2\left(\sigma_o^2 + \sigma_r^2\right)}{N} \\ \sigma_X^2 &= \frac{2\left(\sigma_o^2 + \sigma_r^2\right)}{N} \\ \rho_{XY} &= 0, \end{aligned} \tag{23}$$

such that the probability density function of κ, Equation 21, may be written

$$p\left(\kappa\right) = \frac{e^{\frac{-N}{4\left(\sigma_o^2+\sigma_r^2\right)}}\left(\frac{e^{\frac{N\cos^2\kappa}{4\left(\sigma_o^2+\sigma_r^2\right)}}\sqrt{\pi}\sqrt{N\cos^2\kappa}\left(\operatorname{erf}\left(\frac{1}{2}\sqrt{\frac{N\cos^2\kappa}{\sigma_o^2+\sigma_r^2}}\right)\pm 1\right)}{2\sqrt{\sigma_o^2+\sigma_r^2}} + 1\right)}{2\pi}, \tag{24}$$

where the plus $(+)$ sign is taken when $|\kappa| < \pi/2$ (when $X > 0$), while the minus $(-)$ sign is taken when $\pi > |\kappa| > \pi/2$ (when $X < 0$). Note that with these assumptions, $p(\kappa)$ is independent of the carrier phase offset location of the measurement point ϕ_c.

3 Multi-Point Graphics Model

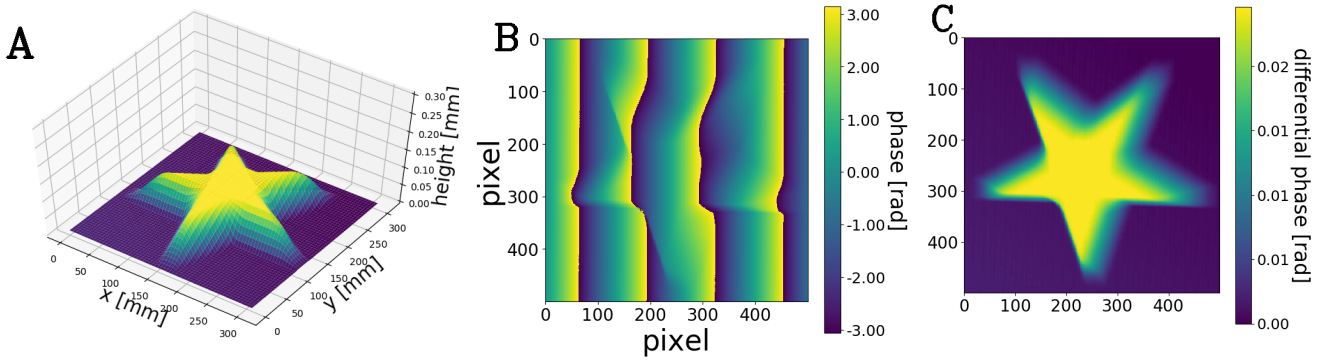

Figure 2: Example images generated by the graphics model. *A* shows the simulated object surface, B shows the wrapped object phase map captured by an offset camera, C shows the differential measured phase map, ϕ.

The phase uncertainty $p(\kappa)$ defined in Section 2 probabilistically quantifies the error in a single-point phase measurement based on pixel intensity noise. In order to ensure its validity for physical DFP measurements, we developed a multi-point graphics model of the physical process including the spatial relationship of projected sinusoidal fringes (carrier phase). The model uses a simulated 3D surface and a simplified pin-hole camera model which can be located anywhere in the scene. The model is constructed to closely parallel the physical process of performing a DFP surface or shape measurement, and to incorporate camera effects. We claim that each measurement pixel in the phase map generated by the graphics model follows the uncertainty model that we have presented in Section 2. Figure 2 shows an example of the capabilities of the graphics model. This is the procedure by which the model produces a simulated phase map:

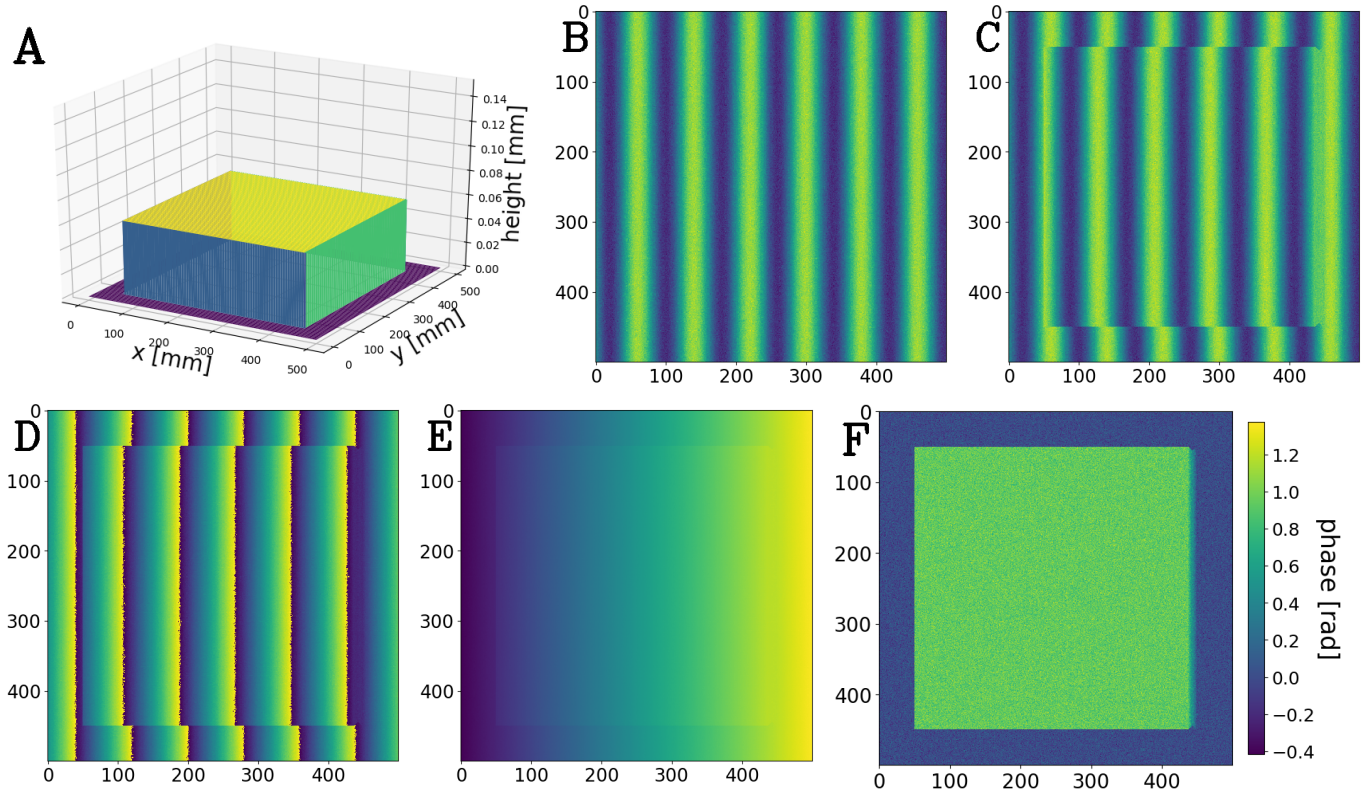

Figure 3: Simulated data progression in the multi-point graphics model. (A) Shows the simulated object surface, which is a raised rectangular area. (B) shows the image of the flat reference plane with simulated fringe projection pattern and uncorrelated random noise, where pixel value is intensity. (C) shows the image of the object surface with simulated fringe projection pattern and uncorrelated random noise, where pixel value is intensity. (D) shows the wrapped phase object image. (E) shows the unwrapped phase object image. (F) shows the final phase difference (or true phase ϕ) map. Simulation parameters including $[R|t]$ and $[A]$ matrices located in the appendix.

1. A plane is constructed as a matrix of 3D points with {X,Y,Z} values, centered on {0,0,0} to serve as the reference surface, and an object surface is defined similarly. In this study, the object surface includes a raised rectangle, apparent in Figure 3. The simulation parameters are located in Table 1 in the Appendix.

2. A camera location is defined in the scene, and its translation and rotation vectors are calculated and combined to construct the extrinsic camera matrix, $[R|t]$, shown below. The intrinsic camera matrix, $[A]$, is defined, containing focal lengths (f_x and f_y), skew (s), and principal point offsets (x_f and y_f), shown in Equations 25 and 26.

$$[R|t] = \left[\begin{array}{ccc|c} r_{1,1} & r_{1,2} & r_{1,3} & t_1 \\ r_{2,1} & r_{2,2} & r_{2,3} & t_2 \\ r_{3,1} & r_{3,2} & r_{3,3} & t_3 \end{array}\right] \tag{25}$$

$$[A] = \begin{bmatrix} f_x & s & x_f \\ 0 & f_y & y_f \\ 0 & 0 & 1 \end{bmatrix} \tag{26}$$

3. Fringe projection parameters are defined such as fringe pitch P and number N of bins used. Since a flat reference plane is used for the present work, P is assumed to be constant throughout the measurement area. Then, to simulate fringe projection, each pixel on the object and reference surface is assigned an intensity value for each bin, I_k based on its spatial location and the projected

fringe pattern. The equation used for fringe pattern intensity generation is located in Table 1 in the Appendix.

4. The world coordinates, {X,Y,Z}, of each point on the reference plane and on the object surface are transformed and scaled using S to pixel coordinates, u, v using

$$S \begin{bmatrix} u \\ v \\ 1 \end{bmatrix} = [A][R|t] \begin{bmatrix} X \\ Y \\ Z \\ 1 \end{bmatrix} \tag{27}$$

5. The pixel coordinates (and their corresponding intensity values) are used to generate a 2-dimensional interpolator. Flat reference and object plane fringe images are generated (now in pixel coordinates) using the interpolator. Pixel intensity noise can be added to the reference and the object images. Examples of these images are shown in Figure 3 B and C.

6. Each set of camera-captured fringe images from both the reference plane and object surface are combined according to Equation 3 to create the reference phase map and object phase map (object phase map shown in Figure 3 D). Both phase maps are unwrapped to remove the 2π discontinuities caused by the arctangent function in Equation 3; the unwrapped object phase map is shown in Figure 3 E. The reference phase map is subtracted from the object phase map, to make the measured phase map ϕ, as seen in Figure 3 F).

In subsequent sections, we use the multi-point graphics model to verify the phase measurement uncertainty distributions derived in Section 2 for a variety of noise conditions.

4 Model Verification & Results

4.1 Model Verification

PDFs of phase uncertainty $p(\kappa)$ from the analytical model were verified against histograms from the multi-point graphics model and histograms of Monte-Carlo based simulations with varying levels of noise correlation, overall standard deviations, and biases. The histograms generated by the multi-point graphics model were constructed by recording the distributions of phase values of a single measurement point over an ensemble of 4,000 separate simulations with unique image noise following the noise structure parameters. We chose a measurement point corresponding to a phase offset of 0, i.e., located at a maximum or minimum intensity "trough" or "crest" of the projected fringes. The Monte-Carlo simulations generated object and reference phase values by adding simulated noise to the intensity terms, I, in Equation 4, representing an example utilizing 4 bins ($N = 4$). In all simulations using the single point phase uncertainty model, ϕ_c was set to 0. The specific simulation parameters for each of the comparisons in Figure 4 are noted in the appendix. Figure 4 compares the analytically derived $p(\kappa)$, histograms of the multi-point graphics model, and histograms from the Monte-Carlo simulations for a variety of noise standard deviations, correlation structure, and biases.

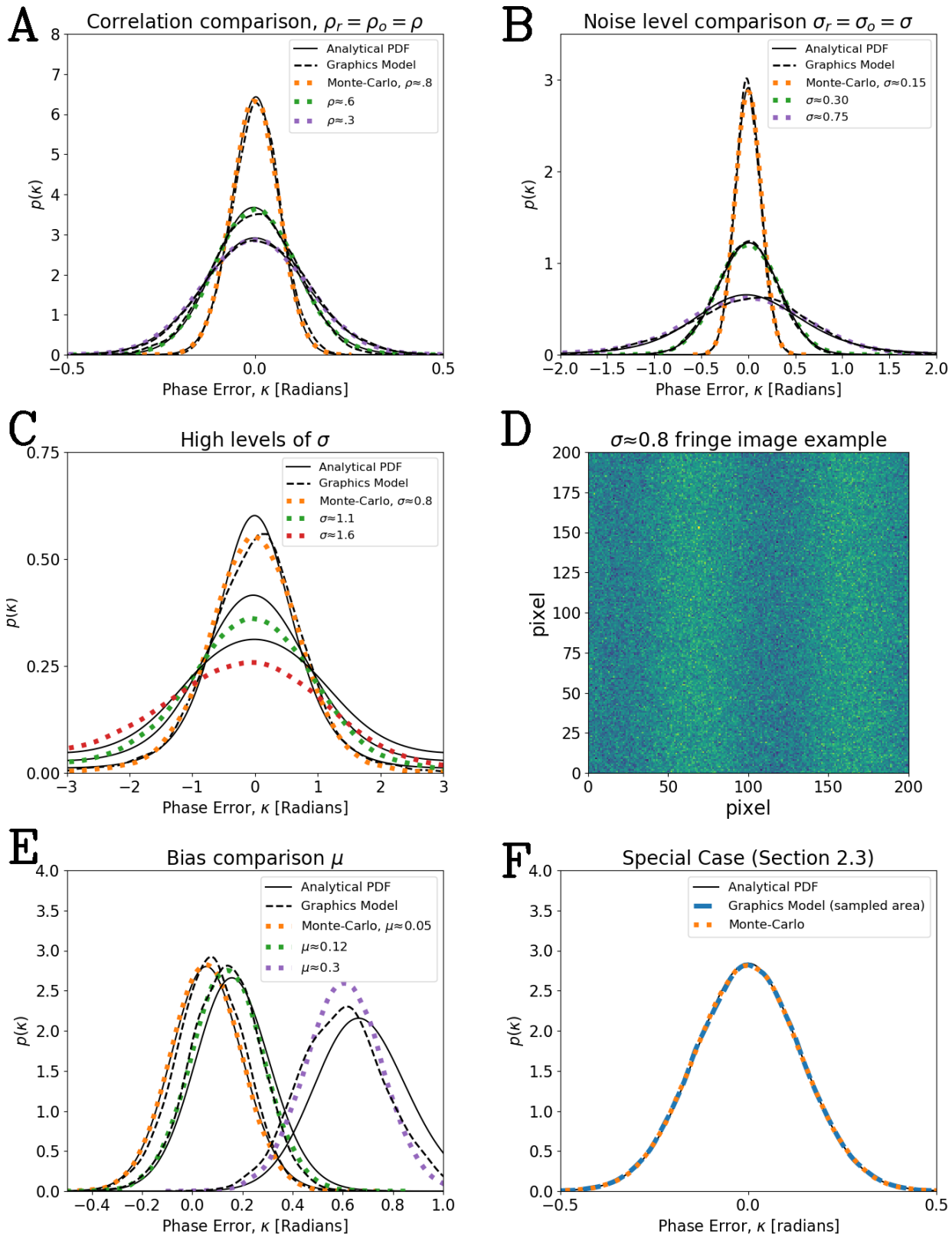

Figure 4: Distributions of analytical phase uncertainty $p(\kappa)$ compared to phase distributions from the multi-point graphics model and Monte-Carlo simulations. (A) shows the comparison for a variety of inter-bin noise correlation $\rho_{r,o}$. (B) shows the comparison for a variety of pixel noise standard deviations in the reference and object images, $\sigma_{r,o}$. (C) shows the levels of pixel noise standard deviation where our approximate model starts to deviate from the Monte-Carlo distributions, due to the neglect of ϵ^2 terms in Equation 10. (D) shows an example fringe pattern from the multi-point graphics model corresponding to a pixel intensity noise standard deviation of 0.8, where our analytical model and graphical model start to diverge from the Monte-Carlo simulations. (E) shows the comparison for a variety of pixel noise bias in the reference and objects images, μ_r and μ_o. (F) shows the comparison of analytical phase uncertainty $p(\kappa)$, histograms of a sampled area from a single simulation of the multi-point graphics model, and Monte-Carlo simulation for noise structured according to the special case in section 2.3.

The expression for $p(\kappa)$ is able to accurately represent the phase distributions observed for single measurement points created from the multi-point graphics model and Monte-Carlo distributions of phase uncertainty across all levels of pixel noise correlation ρ_r, ρ_o and realistic levels of pixel noise, σ_r, σ_o. The analytical $p(\kappa)$, histograms of selected points from the multi-point graphics model, and histograms made by Monte-Carlo simulations are shown in Figure 4A and B. Figure 4C shows the levels of pixel noise which invalidates the assumption made in Equation 10 in which we neglect $\bar{\epsilon}^2$ terms; when $\sigma_r = \sigma_o = \sigma > 0.8$, non-negligible disagreement exists between the analytical model and Monte-Carlo simulations. Phase information produced by the multi-point graphics model also was inaccurate for pixel standard deviations of 0.8 and higher due to numerous unwrapping errors. The figure shows the distributions of the multi-point model for $\sigma \approx 0.8$, but we chose to leave out multi-point phase distributions for higher levels of noise for graph legibility. We argue that in practical application, fringe images with $\sigma << 0.8$ are generally easily obtained with most optical architectures. Figure 4D shows a typical fringe pattern obtained by the multi-point graphics model for a pixel noise standard deviation of 0.8; the fringe pattern is hardly apparent through the pixel noise. This figure is generated with uncorrelated random pixel noise and a fringe pitch of 100 pixels.

Adding biased noise ($\mu_r \neq 0, \mu_o \neq 0$) creates disagreement between the derived phase uncertainty distribution $p(\kappa)$, sampled phase measurement points from the multi-point graphics model, and the Monte-Carlo simulation at smaller levels of σ_r and σ_o (approximately 0.16), as shown in Figure $4E$. We hypothesize that introducing bias creates a non-negligible contribution from the $\bar{\epsilon}^2$ terms which were neglected in Equation 10 which causes the significant disagreement between $p(\kappa)$, the multi-point graphics model, and the Monte-Carlo simulations. Also, biased noise may invalidate the phase reconstruction method (Equation 1), which assumes that the projected fringes are equally spaced across a 2π interval. From an experimental perspective, introducing biased pixel intensity error can represent the physical influences of nonlinear gamma error, where the ideal sinusoidal fringes are distorted, detailed in [29]. This severely affects phase measurement; gamma calibration routines such as gamma interpolation or a gamma look-up-table have been established to linearize the gamma curve of most commercial projectors to ensure optimal sinusoidal fringes.

Figure $4F$ compares $p(\kappa)$ to the sampled phase measurements of the multi-point graphics model and Monte-Carlo simulation. The noise structure of this example corresponds to the special case noise structure described in section 2.3. In contrast to the other verification subplots of Figure 4, the normalized histogram of the multi-point graphics model is built by considering the phase values of many points included in the raised rectangle image corresponding to a single simulation; an image of this surface and resulting phase map is shown in Figure 3. In total, 3,504 points within the raised rectangle were taken from the multi-point graphics model for comparison. We chose to provide this form to show that for a case with the noise assumptions described in the special case, the uncertainty of each measurement point is independent of carrier phase, allowing the comparison of the distribution of phase values inside a measurement area (multi-point graphics model) to the phase uncertainty distribution of a single point $p(\kappa)$.

4.2 Results

To evaluate the effects of the input noise statistical parameters ρ_r, ρ_o, ρ_{or}, σ_r, and σ_o upon the converted phase noise described by $p(\kappa)$, uncertainty surfaces were generated by plotting $p(\kappa)$ as a function of ϕ. First we provide results created by the phase uncertainty analytical model in Figures 5-10. Second, we provide the influence of dual parameter variation on phase uncertainty, shown in Figure 11. The closed-form nature of our phase uncertainty model allows for the formulation of continuous 3-dimensional surfaces describing phase measurement uncertainty distributions $p(\kappa)$ as a function of any of the pixel noise parameters. Each surface is simulated with $\phi_c = 0$ for simplicity, representing analysis on a point with no phase offset from the carrier phase, with other parameters chosen to display the complex range of noise distributions possible. We observed a strongly nonlinear relationship between $p(\kappa)$ and ϕ under most $\sigma_r, \sigma_o, \rho_r, \rho_o, \rho_{or}$ conditions, but we will start with showing a case where $p(\kappa)$ is nearly independent of ϕ. The σ_r and σ_o selections in Figures 5- 10 were selected inside the accuracy bounds of our uncertainty model, and to showcase nonlinear dependence on ϕ of $p(\kappa)$. From a practical standpoint, large variance across bins between σ_r and σ_o can occur when there are temporal noise sources which are non-constant during measurement.

Figure 5 compares the phase uncertainty of noise realizations with constant σ_r and σ_o across bins, with increasing levels of ρ_r and ρ_o, where Figure 5A shows noise generated according to the special case from Section 2.3 (in which $p(\kappa)$ is independent of ϕ). Figures 5B-D show that increasing levels of ρ_r and ρ_o have substantial effect on tightening the dispersion in $p(\kappa)$ but do not contribute substantially to increased ϕ dependence, or any bias. Figures 6 and 7 show the ϕ-dependence of $p(\kappa)$ for noise realizations with identical levels of ρ_r and ρ_o as Figure 5, but with larger variations in σ_r and σ_o. We observed $p(\kappa)$ having a strong periodic dependence on ϕ, proportional to magnitudes of ρ_r, ρ_o in both figure sets. The period of dependence was observed to be π. Figures 6D and 7D show cross sections of the uncertainty surfaces $p(\kappa)$ from noise realized in Figures 6C and 7C. In Figure 6D, $p(\kappa)$ was observed to have low skew and bias at maximum value, generally balanced at $\kappa = 0$. Figure 7D shows that for increased σ_r and σ_o, $p(\kappa)$ exhibited a substantial negative skew and a larger bias in maximum value, for increasing ρ_r and ρ_o. Figure 8 shows $p(\kappa)$ sensitivity to bin index of σ_r, σ_o, i.e. which image (bin) has high or low σ. A-D shows $p(\kappa)$ surfaces with equivalent levels of ρ_r and ρ_o, simply in different orders. We observed that noise realizations with alternating high and low σ_r, σ_o created the largest ϕ dependency, as seen in Figure 8D. Figures 9A-B and 10A-B show $p(\kappa)$ surfaces with varying levels of ρ_{or}, for low and high ρ_r, ρ_o cases, respectively. We observed that the periodic dependency on ϕ was of period 2π; Figures 9C-D and 10C-D show cross-sections of the $p(\kappa)$ surfaces plotted in Figures 9C and 10C with surfaces segmented into $\phi = 0, \pi$ and $\phi = \pi, 2\pi$, respectively. Considerable bias and skew in $p(\kappa)$ was observed in both cases.

We also compared the influence on $p(\kappa)$ of two separate simulation parameters. Figure 11 illustrates the relative effects on $p(\kappa)$ standard deviation of parameters such as σ, N, and ρ. Figure 11A shows the effect of $\sigma_r = \sigma_o = \sigma$ and the number of bins N used for phase measurement on $p(\kappa)$. This figure shows that increasing N can significantly reduce the phase measurement uncertainty. Such a strategy is hence effective for low fringe contrast phase measurements. Figure 11A also be used to determine the number of bins required for a target $p(\kappa)$ structure, with an experimental setup that has an expected (measured) pixel noise standard deviation. While increasing N helps to reduce phase

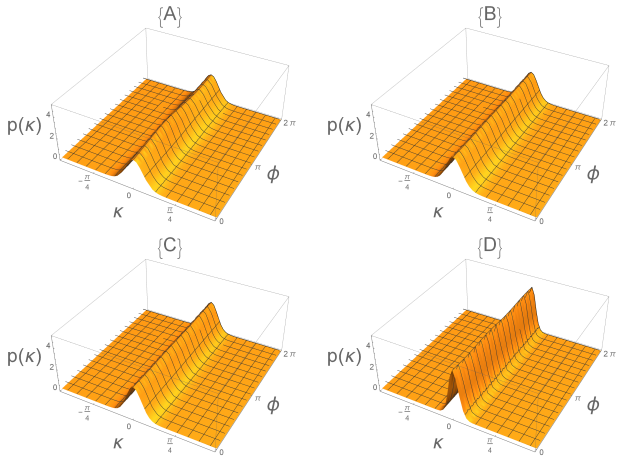

Figure 5: Analytical phase measurement uncertainty distribution surfaces, shown as a function of true phase ϕ. Figures A-D show the effect of increasing inter bin correlation $\rho_o \approx \rho_r$ matrices with off-diagonal terms $\approx 0.001, 0.15, 0.38, 0.62$ in A-D, respectively. Each bin has similar noise standard deviation; $\sigma_r = \{0.1, 0.1, 0.1, 0.1\}$, $\sigma_o = \{0.2, 0.2, 0.2, 0.2\}$.

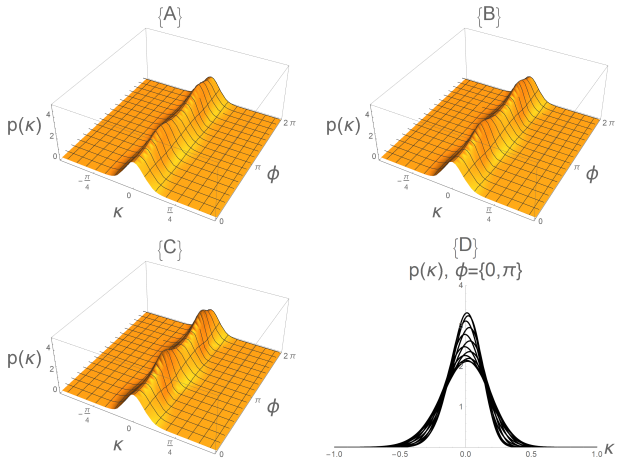

Figure 6: Analytical phase measurement uncertainty distribution surfaces, shown as a function of true phase ϕ. Figures A-C show the effect of increasing inter bin correlation $\rho_o \approx \rho_r$ matrices with off-diagonal terms $\approx 0.15, 0.38, 0.62$ in A-C, respectively. (D) shows $p(\kappa)$ cross sections from (C), for $\phi = k\pi/12, k = 1, 2.., 6$. Noise standard deviation varies across bin index; $\sigma_r = \{0.2, 0.01, 0.01, 0.2\}$, $\sigma_o = \{0.3, 0.02, 0.01, 0.2\}$.

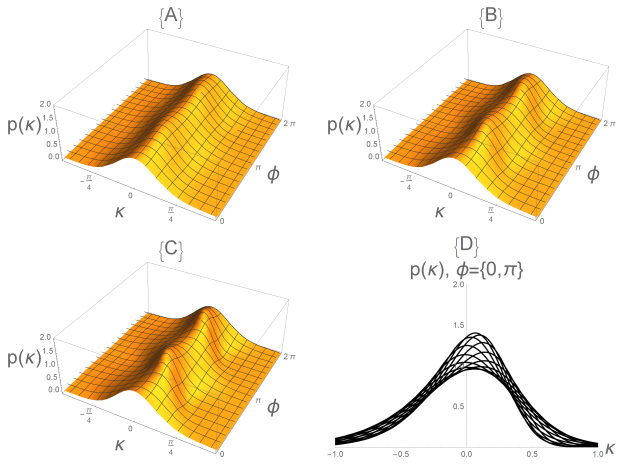

Figure 7: Analytical phase measurement uncertainty distribution surfaces, shown as a function of true phase ϕ. Figures A-C show the effect of increasing inter-bin correlation $\rho_o \approx \rho_r$ matrices with off-diagonal terms $\approx 0.15, 0.38, 0.62$ in A-C, respectively. (D) shows $p(\kappa)$ cross sections from (C), for $\phi = k\pi/12, k = 1, 2.., 12$. Noise standard deviation varies substantially across bin index; $\sigma_r = \{0.5, 0.03, 0.03, 0.5\}$, $\sigma_o = \{0.6, 0.04, 0.01, 0.5\}$.

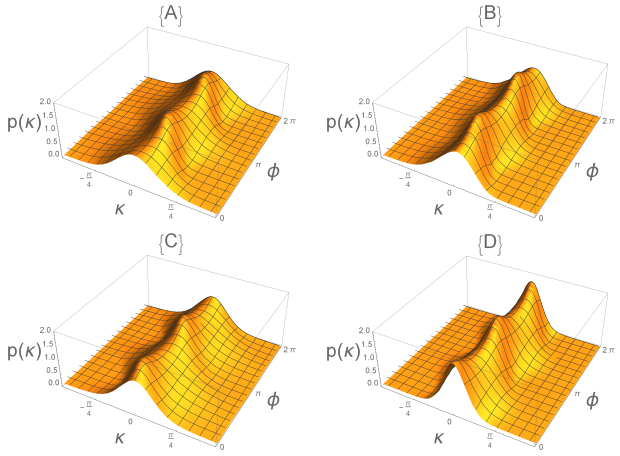

Figure 8: Analytical phase measurement uncertainty distribution surfaces, shown as a function of true phase ϕ. Figures A-D show the effect of changing the bin-index of low and large noise standard deviations. Noise correlation matrices are constant across A-D, with off-diagonal terms of $\rho_o = \rho_r \approx 0.6$. Noise standard deviation for
(A): $\sigma_r = \{0.5, 0.03, 0.03, 0.5\}, \sigma_o = \{0.6, 0.04, 0.01, 0.5\}$,
(B): $\sigma_r = \{0.03, 0.5, 0.5, 0.03\}, \sigma_o = \{0.6, 0.04, 0.5, 0.01\}$,
(C): $\sigma_r = \{0.5, 0.5, 0.03, 0.03\}, \sigma_o = \{0.04, 0.01, 0.5, 0.6\}$,
(D): $\sigma_r = \{0.5, 0.03, 0.5, 0.03\}, \sigma_o = \{0.04, 0.6, 0.01, 0.5\}$.

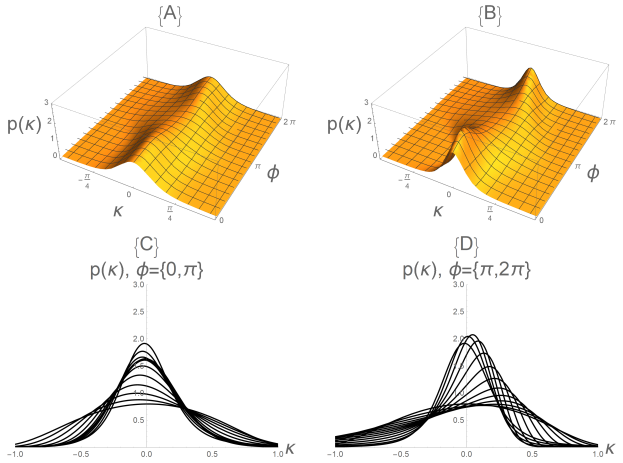

Figure 9: Analytical phase measurement uncertainty distribution surfaces, shown as a function of true phase ϕ. Figures A-B show the effect of increasing reference-object correlation ρ_{or} matrices with off-diagonal terms $\approx 0.32, 0.64$, respectively. The reference and object images have low correlation; matrices ρ_o and ρ_r off diagonal terms ≈ 0.18 for A-B. C-D shows $p(\kappa)$ cross sections from (B), for $\phi = k\pi/12$, and $\phi = \pi + k\pi/12, k = 1, 2, 3..., 12$, respectively. Noise standard deviation varies substantially across bin index; $\sigma_r = \{0.5, 0.03, 0.03, 0.5\}$, $\sigma_o = \{0.6, 0.04, 0.01, 0.5\}$.

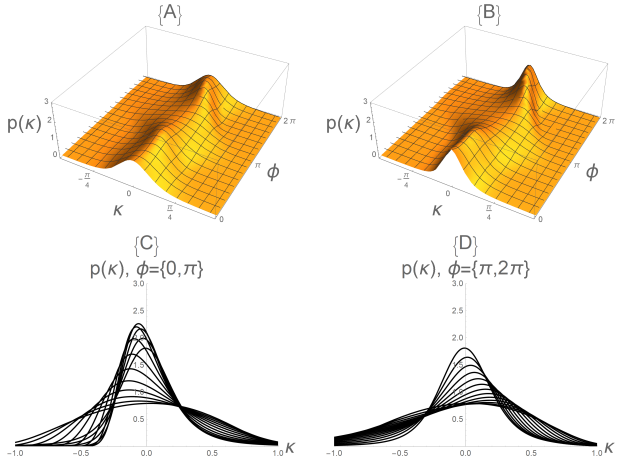

Figure 10: Analytical phase measurement uncertainty distribution surfaces, shown as a function of true phase ϕ. Figures A-B show the effect of increasing reference-object correlation ρ_{or} matrices with off-diagonal terms $\approx 0.32, 0.64$, respectively. The reference and object images have high correlation; matrices ρ_o and ρ_r off diagonal terms ≈ 0.73 for A-B. C-D shows $p(\kappa)$ cross sections from (B), for $\phi = k\pi/12$, and $\phi = \pi + k\pi/12, k = 1, 2, 3..., 12$, respectively. Noise standard deviation varies substantially across bin index; $\sigma_r = \{0.5, 0.03, 0.03, 0.5\}$, $\sigma_o = \{0.6, 0.04, 0.01, 0.5\}$.

uncertainty, it does have asymptotic behavior for large N. Figure 11B shows the diagonal-symmetric effects of increasing ρ_r and ρ_o on $p(\kappa)$ standard deviation. As already indicated by Figure 5, $p(\kappa)$ tightens proportionally to ρ_r, ρ_o; Figure 11B shows that the tightening contributions from ρ_r and ρ_o are equivalent. Figures 11C and 11D show $p(\kappa)$ standard deviation and $p(\kappa)$ mean, respectively. The similarities in period and overall shape trends of 11C and 11D suggest correlation between $p(\kappa)$ standard deviation and $p(\kappa)$ mean. This relationship may be explored in future papers, but is deemed out of the scope for the current work.

5 Conclusion & Future Work

An analytical model was derived to describe single-point phase measurement uncertainty caused by pixel intensity noise. The model was developed in order to advance DFP surface measurement capability by adding a statistical model to provide measurable confidence levels for the phase measurement of each pixel. We envision that by measuring the noise statistics of each pixel, any existing DFP system can be modified to provide phase maps with statistical confidences embedded. We verified our model by comparing the derived phase measurement uncertainty distributions to normalized histograms of phase values generated by a novel, multi-point graphics model and from Monte-Carlo simulations. The model was verified using a wide range of noise realizations with varying levels of correlation, noise levels, and bias levels. We observed excellent agreement across pixel intensity noise correlation and pixel noise standard deviations that we argue are realistic in physical measurements. When adding biased noise, we observed a disagreement between the derived phase uncertainty, multi-point graphics model, and the Monte-Carlo simulations which we attribute to two reasons: (1) bias creates a factor which

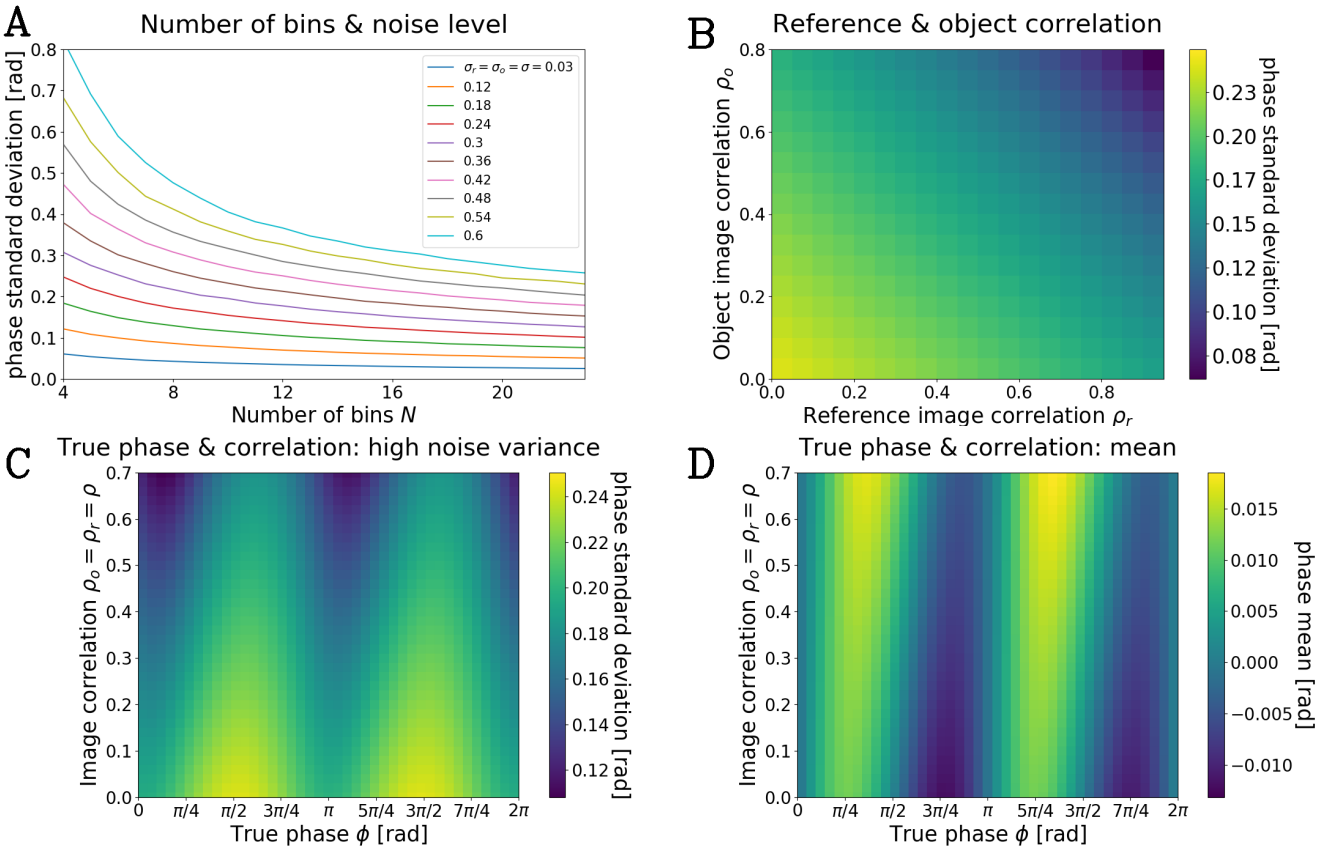

Figure 11: Monte-Carlo simulations of phase measurement uncertainty with 2 varying parameters. Pixel intensity corresponds to the phase uncertainty distribution standard deviation. Figure (A) shows how phase uncertainty is affected by object pixel intensity standard deviation σ_o and the number of bins used for phase measurement N. Figure (B) shows the symmetry of reference image noise correlation ρ_r and object image noise correlation ρ_o on phase uncertainty distribution standard deviation. Figures (C) and (D) show phase uncertainty distribution standard deviation and phase uncertainty distribution mean, respectively, as functions of true phase ϕ. The y-axis on both Figures (C) and (D) represent off diagonal terms of the inter-bin correlation matrices.

cannot be neglected in the assumption of Equation 10, and (2) bias alters the center intensity value of each bin pixel, invalidating the phase reconstruction method (Equation 4). The model verification are shown in Figure 4. In order to highlight the nonlinear and "un-intuitive" nature of phase uncertainty, the analytical model was used to generate continuous phase uncertainty surfaces (see Figures 5-10) where we explored the sensitivity of phase uncertainty to varying noise statistics including inter-bin reference and object correlation, and variations in noise standard deviation. The analytical model was also used to generate two-axis parameter studies, where we observed the relative effect of two parameters simultaneously (including number of bins N, pixel noise standard deviation (σ_r, σ_o), and pixel noise correlation (ρ_r, ρ_o)) on phase uncertainty levels and bias. r4c55 r4c56

This was the first to explicitly determine error propagation of pixel noise in the DFP measurement technique, and provided a statistical estimation of phase measurement uncertainty for each point of measurement. Advancement of this model currently includes work involving (1) further developing the analytical model to include phase-to-height measurement uncertainty, (2) developing a relationship between projection parameters (such as camera position, fringe pitch, number of bins, etc.) and phase error statistics, to optimize the experimental setup, (3) exploring filtering techniques for full field phase mapping using the graphics model, and (4) comparing the uncertainty distribution from the analytical model to sampling pixel-by-pixel phase surface measurements to test the efficacy of estimation.

Acknowledgements

This research was funded by Los Alamos National Laboratory (LANL) through the Engineering Institute - a research and education collaboration between LANL and the University of California San Diego's Jacobs School of Engineering. This collaboration seeks to promote multidisciplinary engineering research that develops and integrates advanced predictive modeling, novel sensing systems, and new developments in information technology to address LANL mission relevant problems. LA-UR-20-22772.

6 Appendix: simulation parameters

Parameter	**Quantity**
height of raised area ϕ	0.6 [mm]
Number of bins N	4 [bins]
Fringe period P	80 [mm]
Fringe intensity I	$I = \frac{255}{2}(1 + \cos(\frac{2\pi x}{P} + \delta_k))$
Camera location [-]	{200, 0, 1000} [mm]
Extrinsic camera matrix $[R\|t]$	$\begin{pmatrix} -10 & 0 & 0 & 0 \\ 0 & 9.806 & -1.961 & 0 \\ 0 & 0.402 & 1. & 0 \\ 0 & -0.196 & -0.981 & 1019.8 \end{pmatrix}$
Intrinsic camera matrix $[A]$	$\begin{pmatrix} 10 & 0 & 250 \\ 0 & 10 & 250 \\ 0 & 0 & 1. \end{pmatrix}$
Reference and object pixel noise std. $\sigma_{r,o}$	{0.1, 0.1, 0.1, 0.1}

Table 1: Figure 3 Simulation Parameters

Parameter	**Quantity**
Phase ϕ	1.885 [rad]
Number of bins N	4 [bins]
Monte-Carlo realizations [-]	49152 [realizations]
Reference pixel noise std. σ_r	{0.125, 0.151, 0.15, 0.28}
Object pixel noise std. σ_o	{0.144, 0.147, 0.13, 0.18}
Reference pixel noise correlation ρ_r	$\begin{pmatrix} 1. & 0.201 & 0.206 & 0.094 \\ 0.201 & 1. & 0.402 & 0.301 \\ 0.206 & 0.402 & 1. & 0.277 \\ 0.094 & 0.301 & 0.277 & 1. \end{pmatrix}, \begin{pmatrix} 1. & 0.601 & 0.493 & 0.594 \\ 0.601 & 1. & 0.54 & 0.4 \\ 0.493 & 0.54 & 1. & 0.768 \\ 0.594 & 0.4 & 0.768 & 1. \end{pmatrix}, \begin{pmatrix} 1. & 0.69 & 0.773 & 0.859 \\ 0.69 & 1. & 0.855 & 0.695 \\ 0.773 & 0.855 & 1. & 0.769 \\ 0.859 & 0.695 & 0.769 & 1. \end{pmatrix}$
Object pixel noise correlation ρ_o	$\begin{pmatrix} 1. & 0.296 & 0.251 & 0.1 \\ 0.296 & 1. & 0.331 & 0.202 \\ 0.251 & 0.331 & 1. & 0.293 \\ 0.1 & 0.202 & 0.293 & 1. \end{pmatrix}, \begin{pmatrix} 1. & 0.597 & 0.501 & 0.599 \\ 0.597 & 1. & 0.401 & 0.5 \\ 0.501 & 0.401 & 1. & 0.503 \\ 0.599 & 0.5 & 0.503 & 1. \end{pmatrix}, \begin{pmatrix} 1. & 0.885 & 0.751 & 0.785 \\ 0.885 & 1. & 0.774 & 0.895 \\ 0.751 & 0.774 & 1. & 0.651 \\ 0.785 & 0.895 & 0.651 & 1. \end{pmatrix}$

Table 2: Figure 4 *a* Simulation Parameters

Parameter	**Quantity**
Phase ϕ	1.885 [rad]
Number of bins N	4 [bins]
Monte-Carlo realizations [-]	49152 [realizations]
Reference pixel noise std. σ_r	{0.125, 0.151, 0.15, 0.279}, {0.391, 0.33, 0.379, 0.436},{0.591, 0.63, 0.579, 0.736}
Object pixel noise std. σ_o	{0.144, 0.147, 0.13, 0.18},{0.252, 0.324, 0.212, 0.368},{0.752, 0.623, 0.713, 0.869}
Reference pixel noise correlation $_{\rho_r}$	$\begin{pmatrix} 1. & 0.201 & 0.206 & 0.094 \\ 0.201 & 1. & 0.402 & 0.301 \\ 0.206 & 0.402 & 1. & 0.277 \\ 0.094 & 0.301 & 0.277 & 1. \end{pmatrix}$
Object pixel noise correlation $_{\rho_o}$	$\begin{pmatrix} 1. & 0.296 & 0.251 & 0.1 \\ 0.296 & 1. & 0.331 & 0.202 \\ 0.251 & 0.331 & 1. & 0.293 \\ 0.1 & 0.202 & 0.293 & 1. \end{pmatrix}$

Table 3: Figure 4 *b* Simulation Parameters

Parameter	**Quantity**
Phase ϕ	1.885 [rad]
Number of bins N	4 [bins]
Monte-Carlo realizations [-]	49152 [realizations]
Reference pixel noise std. σ_r	{0.537, 0.546521, 0.5372, 0.54624}, {0.7125, 0.83151, 0.715, 0.828}, {1.125, 1.151, 1.115, 1.18}, {1.625, 1.651, 1.615, 1.58}
Object pixel noise std. σ_o	{0.537152, 0.545176, 0.54504, 0.540144}, {0.7144, 0.8147, 0.813, 0.7518},{1.144, 1.147, 1.13, 1.18},{1.644, 1.647, 1.53, 1.78}
Reference pixel noise correlation ρ_r	$\begin{pmatrix} 1. & 0.201 & 0.206 & 0.094 \\ 0.201 & 1. & 0.402 & 0.301 \\ 0.206 & 0.402 & 1. & 0.277 \\ 0.094 & 0.301 & 0.277 & 1. \end{pmatrix}$
Object pixel noise correlation ρ_o	$\begin{pmatrix} 1. & 0.296 & 0.251 & 0.1 \\ 0.296 & 1. & 0.331 & 0.202 \\ 0.251 & 0.331 & 1. & 0.293 \\ 0.1 & 0.202 & 0.293 & 1. \end{pmatrix}$

Table 4: Figure 4 *c* Simulation Parameters

Parameter	Quantity
Phase ϕ	1.885 [rad]
Number of bins N	4 [bins]
Monte-Carlo realizations [-]	49152 [realizations]
Reference pixel noise std. σ_r	{0.125, 0.151, 0.15, 0.28}
Object pixel noise std. σ_o	{0.144, 0.147, 0.13, 0.18}
Reference pixel noise biases μ_r	{0., 0.054, 0., -0.058},{0., 0.145, 0., -0.134},{-0.245, 0.35, -0.331, 0.135}
Object pixel noise biases μ_o	{0., 0.068, 0., -0.048},{0., 0.135, 0., -0.175},{0.251, 0.35, -0.54, -0.35}
Reference pixel noise correlation ρ_r	$\begin{pmatrix} 1. & 0.201 & 0.206 & 0.094 \\ 0.201 & 1. & 0.402 & 0.301 \\ 0.206 & 0.402 & 1. & 0.277 \\ 0.094 & 0.301 & 0.277 & 1. \end{pmatrix}$
Object pixel noise correlation ρ_o	$\begin{pmatrix} 1. & 0.296 & 0.251 & 0.1 \\ 0.296 & 1. & 0.331 & 0.202 \\ 0.251 & 0.331 & 1. & 0.293 \\ 0.1 & 0.202 & 0.293 & 1. \end{pmatrix}$

Table 5: Figure 4 *e* Simulation Parameters

Parameter	Quantity
Phase ϕ	1.885 [rad]
Number of bins N	4 [bins]
Monte-Carlo realizations [-]	250,000 [realizations]
Reference pixel noise std. σ_r	{0.13, 0.13, 0.13, 0.13}
Object pixel noise std. σ_o	{0.15, 0.15, 0.15, 0.15}

Table 6: Figure 4 *f* Simulation Parameters

References

[1] S. S. Gorthi and P. Rastogi, "Fringe projection techniques: whither we are?," Optics and Lasers in Engineering, vol. 48, no. IMAC-REVIEW-2009-001, pp. 133–140, 2010.

[2] K. J. Gasvik, "Moire technique by means of digital image processing," Applied Optics, vol. 22, no. 22, pp. 3543–3548, 1983.

[3] R. E. Brooks and L. O. Heflinger, "Moiré gauging using optical interference patterns," Applied Optics, vol. 8, no. 5, pp. 935–939, 1969.

[4] C. A. Sciammarella, L. Lamberti, and A. Boccaccio, "General model for moiré contouring, part 1: theory," Optical Engineering, vol. 47, no. 3, p. 33605, 2008.

[5] C. A. Sciammarella, L. Lamberti, A. Boccaccio, E. Cosola, and D. Posa, "General model for moiré contouring, part 2: applications," Optical Engineering, vol. 47, no. 3, p. 33606, 2008.

[6] C. A. Sciammarella, L. Lamberti, A. Boccaccio, and F. M. Sciammarella, "High precision contouring with moiré and related methods: a review," Strain, vol. 47, pp. 43–64, 2011.

[7] A. E. Ennos, "Measurement of in-plane surface strain by hologram interferometry," Journal of Physics E: Scientific Instruments, vol. 1, no. 7, p. 731, 1968.

[8] D. Léger and J. C. Perrin, "Real-time measurement of surface roughness by correlation of speckle patterns," Journal of Optical Society of America, vol. 66, no. 11, pp. 1210–1217, 1976.

[9] C. J. Moore, D. R. Burton, O. Skydan, P. J. Sharrock, and M. Lalor, "3D body surface measurement and display in radiotherapy part I: Technology of structured light surface sensing," in International Conference on Medical Information Visualisation-BioMedical Visualisation (MedVis' 06), pp. 97–102, IEEE, 2006.

[10] F. Lilley, M. J. Lalor, and D. R. Burton, "Robust fringe analysis system for human body shape measurement," Optical Engineering, vol. 39, pp. 187–195, 2000.

[11] K. Genovese and C. Pappalettere, "Whole 3D shape reconstruction of vascular segments under pressure via fringe projection techniques," Optics and Lasers in Engineering, vol. 44, no. 12, pp. 1311–1323, 2006.

[12] P.-R. Jang, R. Arunkumar, T. Leone, Z. Long, M. A. Mott, O. P. Norton, W. P. Okhuysen, Y. Su, D. L. Monts, and P. G. Kirk, "Quantitative imaging characterization of aluminum pit corrosion in Oak Ridge research reactor pool," in Advanced Environmental, Chemical, and Biological Sensing Technologies IV, vol. 6377, p. 63770S, International Society for Optics and Photonics, 2006.

[13] P. S. Huang, F. Jin, and F.-P. Chiang, "Quantitative evaluation of corrosion by a digital fringe projection technique," Optics and Lasers in Engineering, vol. 31, no. 5, pp. 371–380, 1999.

[14] R. Ernst, A. Weckenmann, and R. Velgan, "Local wall thickness measurement of formed sheet metal using fringe projection technique," in XVII IMEKO World Congress, Metrology in the 3rd Millennium. Croatia, pp. 1802–1805, Citeseer, 2003.

[15] C. Quan, C. J. Tay, X. Y. He, X. Kang, and H. M. Shang, "Microscopic surface contouring by fringe projection method," Optics and Laser Technology, vol. 34, no. 7, pp. 547–552, 2002.

[16] X. Y. He, W. Sun, X. Zheng, and M. Nie, "Static and dynamic deformation measurements of micro beams by the technique of digital image correlation," in Key Engineering Materials, vol. 326, pp. 211–214, 2006.

[17] H. Guo, H. He, and M. Chen, "Gamma correction for digital fringe projection profilometry," Applied Optics, vol. 43, no. 14, pp. 2906–2914, 2004.

[18] S. Ma, C. Quan, R. Zhu, L. Chen, B. Li, and C. J. Tay, "A fast and accurate gamma correction based on Fourier spectrum analysis for digital fringe projection profilometry," Optics Communications, vol. 285, no. 5, pp. 533–538, 2012.

[19] T. Hoang, B. Pan, D. Nguyen, and Z. Wang, "Generic gamma correction for accuracy enhancement in fringe-projection profilometry," Optics Letters, vol. 35, no. 12, pp. 1992–1994, 2010.

[20] Y. Hu, J. Xi, Z. Yang, E. Li, and J. F. Chicharo, "Study on generalized analysis model for fringe pattern profilometry," IEEE Transactions on Instrumentation and Measurement, vol. 57, no. 1, pp. 160–167, 2007.

[21] L.-C. Chen and C.-C. Liao, "Calibration of 3D surface profilometry using digital fringe projection," Measurement Science and Technology, vol. 16, no. 8, p. 1554, 2005.

[22] Z. Lei, C. Wang, and C. Zhou, "Multi-frequency inverse-phase fringe projection profilometry for nonlinear phase error compensation," Optics and Lasers in Engineering, vol. 66, pp. 249–257, 2015.

[23] T. Maack and R. Kowarschik, "Camera influence on the phase-measurement accuracy of a phase-shifting speckle interferometer," Applied optics, vol. 35, no. 19, pp. 3514–3524, 1996.

[24] P. S. Huang, Q. J. Hu, and F.-P. Chiang, "Double three-step phase-shifting algorithm," Applied optics, vol. 41, no. 22, pp. 4503–4509, 2002.

[25] J. Pan, P. S. Huang, and F.-P. Chiang, "Color-coded binary fringe projection technique for 3-D shape measurement," Optical Engineering, vol. 44, no. 2, p. 23606, 2005.

[26] G. H. Notni and G. Notni, "Digital fringe projection in 3D shape measurement: an error analysis," in Optical Measurement Systems for Industrial Inspection III, vol. 5144, pp. 372–380, International Society for Optics and Photonics, 2003.

[27] J. Molimard and L. Navarro, "Uncertainty on fringe projection technique: A Monte-Carlo-based approach," Optics and Lasers in Engineering, vol. 51, no. 7, pp. 840–847, 2013.

[28] M. Halioua and H.-C. Liu, "Optical three-dimensional sensing by phase measuring profilometry," Optics and Lasers in Engineering, vol. 11, no. 3, pp. 185–215, 1989.

[29] S. Zhang, High-Speed 3D Imaging with Digital Fringe Projection Techniques. CRC Press, USA, 2016.

[30] A. K. Jain, Fundamentals of Digital Image Processing. Englewood Cliffs, NJ: Prentice Hall,, 1989.

[31] J. Takamatsu, Y. Matsushita, and K. Ikeuchi, "Estimating camera response functions using probabilistic intensity similarity," in 2008 IEEE Conference on Computer Vision and Pattern Recognition, pp. 1–8, IEEE, 2008.

[32] B. Pan, K. Li, and W. Tong, "Fast, robust and accurate digital image correlation calculation without redundant computations," Experimental Mechanics, vol. 53, no. 7, pp. 1277–1289, 2013.